Front. Phys., 2013, 8(2): 228–235
DOI 10.1007/s11467-013-0289-9

RESEARCH ARTICLE

Coherent control of dressed images of four-wave mixing

Zhen-Kun Wu[1], **Yi-Qi Zhang**[1], **Tai-Kun Liu**[1], **Zhao-Yang Zhang**[1], **Cheng Li**[1], **Yan-Peng Zhang**[1,*], **Min Xiao**[2,3,†]

[1] *Key Laboratory for Physical Electronics and Devices of the Ministry of Education & Shaanxi Key Lab of Information Photonic Technique, Xi'an Jiaotong University, Xi'an 710049, China*

[2] *Department of Physics, University of Arkansas, Fayetteville, Arkansas 72701, USA*

[3] *National Laboratory of Solid State Microstructures and Department of Physics, Nanjing University, Nanjing 210093, China*

*E-mail: *ypzhang@mail.xjtu.edu.cn, †mxiao@uark.edu*

Received January 9, 2013; accepted January 15, 2013

In two-level as well as V-type three-level atomic systems, we study probe transmission, four-wave mixing (FWM) and fluorescence signals with dressing effect experimentally and theoretically. We find both the hyperfine structure (at the same energy level) and the transition dipole moment (at different energy levels) can affect the dressing effect. We also experimentally investigate that angle-control dynamics in the nonlinear propagation of the images of the probe and generated FWM in two-level atomic systems, and find that the focusing and defocusing of probe beam and FWM signals can be greatly affected by the angles between dressing fields.

Keywords four-wave mixing, fluorescence, dressing effect, Kerr effect

PACS numbers 42.65.Tg, 42.65.Jx, 45.65.Sf, 42.50.Gy

1 Introduction

In past decades, electromagnetically induced transparency (EIT) attracts a lot of attention for its special properties on reducing the absorption of a beam when it passes through the multi-level atomic vapors [1–4]. Meanwhile, it is found that the nonlinearity of the medium can be enhanced strongly by the laser induced atomic coherence [1, 2], which plays a key role in producing the efficient four-wave mixing (FWM) processes and large refractive index modulation [3]. Among so many studies in this area, destructive and constructive interferences in a two-level atomic system [5] and competition between two coexisting FWM processes via atomic coherence in a four-level atomic system [6] have been reported. Recently, the interactions of doubly dressed states and the corresponding effects in atomic systems are quite involved [7, 8] and some progress is reported. For example, in an EIT system, the interaction between double-dark states and splitting of a dark state in a four-level atomic system was studied theoretically [7]; the existence of the secondarily dressed states was verified through the observation of triple-peaks absorption spectrum in the N-type cold atomic system [8]. In the past few years, our research group has theoretically investigated three types of doubly dressed schemes in a five-level atomic system [9] and observed three peak Autler–Townes (AT) splitting of the secondary dressed FWM signal [10]. In addition, we have also observed the evolution of the intensity enhancement and suppression in FWM signal spectrum by controlling additional laser fields [11]. On the other hand, accompanying the FWM process, there will be fluorescence signals that can be induced by spontaneous emission under EIT conditions [12, 13], and some investigations were proceeded [14, 15] on this topic for its potential applications in metrology and long-distance quantum communication and quantum correlation.

In this paper, we adopt V-type three-level atomic systems and two-level atomic systems, in which we first experimentally investigate the properties of probe transmission, FWM and fluorescence signals with dressing effects, and then discuss the phenomena observed in the two different systems in detail. At the same time, we will show the influence on the dressing effect from dipole moment and hyperfine structures. As a last research topic of this paper, we will also study the influence on the

images and intensities of probe transmission and FWM signals brought by the angles between dressing fields in two-level atomic systems. The organization of the paper is: in Section 2, we introduce the theoretical model, experimental setup, and show the physical quantities used in the paper; in Section 3, we analyze and discuss the experimental results in the two systems; in Section 4, we conclude the paper.

2 Theoretical model and experimental setup

Two experimentally involved sodium atomic systems are shown in Fig. 1(a) and (b), respectively. The energy levels of $|0\rangle$ $(3S_{1/2})$,$|1\rangle$ $(3P_{1/2})$ and $|2\rangle$ $(3P_{3/2})$ form a Na V-type three-level atomic system. The experimental setup and the spatially aligned laser beams are shown in Fig. 1(c) and (d), respectively. The probe beam ($\boldsymbol{E}_3$) propagates opposite to $\boldsymbol{E}_1$, while the two couples of pump beams $\boldsymbol{E}_1$&$\boldsymbol{E}_2$ (along the same direction) and $\boldsymbol{E}_1'$&$\boldsymbol{E}_2'$ (along the same direction) both have a small angles (0.3°) with $\boldsymbol{E}_1$ in x–z plane and y–z plane, respectively. If level $|1\rangle$ is not used, the system is a two-level system, as shown in Fig. 1(a), that the beams $\boldsymbol{E}_1$, $\boldsymbol{E}_1'$, and $\boldsymbol{E}_3$ (Rabi frequencies are G_1, G_1', and G_3, respectively) all connect transition $|0\rangle - |2\rangle$ have same frequency ω_1, and generate an efficient degenerate FWM (DFWM) signal $\boldsymbol{E}_{\mathrm{F1}}$ satisfying the phase matching condition $\boldsymbol{k}_{\mathrm{F1}} = \boldsymbol{k}_1 - \boldsymbol{k}_1' + \boldsymbol{k}_3$. The beams $\boldsymbol{E}_2$ and $\boldsymbol{E}_2'$ (G_2 and G_2', respectively) that also connect $|0\rangle - |2\rangle$ have same frequency ω_2 and induce a nondegenerate FWM (NDFWM) $\boldsymbol{E}_{\mathrm{F2}}$ satisfying $\boldsymbol{k}_{\mathrm{F2}} = \boldsymbol{k}_3 + \boldsymbol{k}_2 - \boldsymbol{k}_2'$. If the five laser beams are all on, another two NDFWM processes $\boldsymbol{E}_{\mathrm{F3}}$ ($\boldsymbol{k}_{\mathrm{F3}} = \boldsymbol{k}_2 - \boldsymbol{k}_1' + \boldsymbol{k}_3$) and $\boldsymbol{E}_{\mathrm{F4}}$ ($\boldsymbol{k}_{\mathrm{F4}} = \boldsymbol{k}_1 - \boldsymbol{k}_2' + \boldsymbol{k}_3$) can be obtained along the directions of $\boldsymbol{E}_{\mathrm{F1}}$ and $\boldsymbol{E}_{\mathrm{F2}}$, respectively. It is worth mentioning, the fluorescence signals $\rho_{22}^{(2)}$ and $\rho_{22}^{(4)}$ can be produced when the system decays from $|2\rangle$. In this experiment, we define the reduced angle between $\boldsymbol{E}_2$ and $\boldsymbol{E}_2'$ as $\Delta\theta_2 = \theta_{2y} - \theta_{2y0}$, where θ_{2y} is the angle between $\boldsymbol{E}_2$ and $\boldsymbol{E}_2'$ in y–z plane, and θ_{2y0} the angle when the intersecting point between $\boldsymbol{E}_2$ and $\boldsymbol{E}_2'$ reach the center of the pipe oven. In Fig. 1(d), when the intersecting point moves from the point C (the back of the heat pipe oven) to the position A (the front of the heat pipe oven), the value of $\Delta\theta_2$ changes from −0.15 to 0.15.

When $\boldsymbol{E}_2$ and $\boldsymbol{E}_2'$ are tuned to $|0\rangle - |1\rangle$, and $\boldsymbol{E}_1$, $\boldsymbol{E}_1'$ and $\boldsymbol{E}_3$ connect $|0\rangle - |2\rangle$, the system becomes V-type three-level, as shown in Fig. 1(b). In such system, there will be an efficient DFWM signal $\boldsymbol{E}_{\mathrm{F1}}$ and a NDFWM signal $\boldsymbol{E}_{\mathrm{F2}}$ with two groups of fluorescence signals decaying from $|1\rangle(\rho_{11}^{(2)}$ and $\rho_{11}^{(4)})$ and $|2\rangle(\rho_{22}^{(2)}$ and $\rho_{22}^{(4)})$, respectively.

2.1 Dressed state theory in the two-level atomic system

In order to interpret the following experimental results,

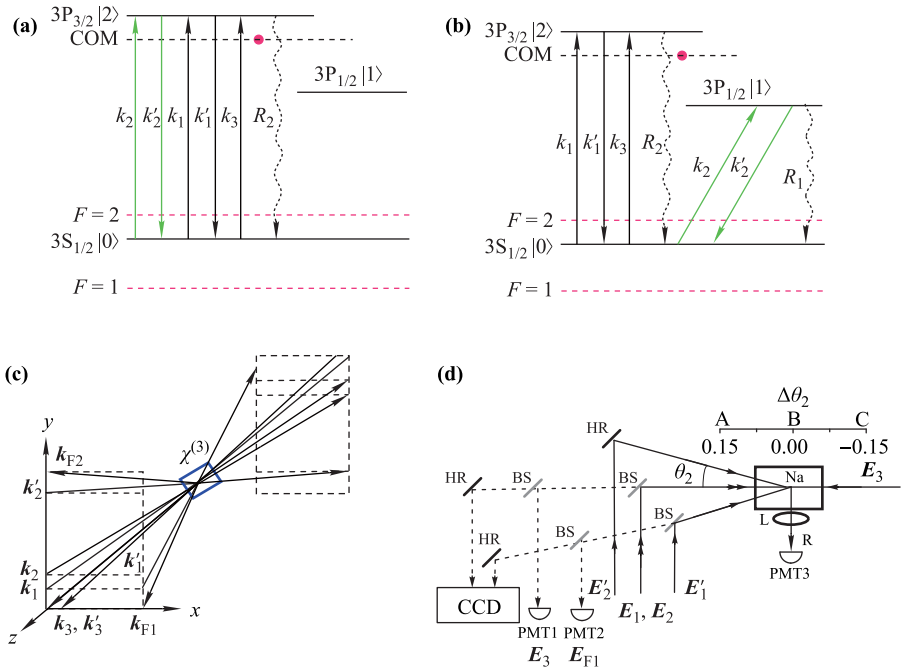

Fig. 1 **(a)** two energy-level system diagram between $|0\rangle$ and $|2\rangle$, corresponding to wavelengths of 589.0 nm. **(b)** V-type energy-level system diagrams, the wavelength of one dye laser beams is 589.0 nm, and the other is 589.6 nm. **(c)** and **(d)** Spatial geometry for the laser beams in the experiment and experimental setup, respectively. The scale gives the angle value of the corresponding position in heat pipe oven as shown in (d). Every optical element can be signified as: HR – High reflective mirror, BS – Beam splitter (50%), L – Convex lens, PMT – Photomultiplier tube.

we perform the theoretical calculation on probe transmission, $\boldsymbol{E}_{\rm F1}$ and fluorescence process in the two-level atomic system. For $\boldsymbol{E}_{\rm F1}$, its generation process can be viewed as a series of transitions steps. The first step is a rising transition $|0\rangle \rightarrow |2\rangle$ with absorption of a pump photon $\boldsymbol{E}_1$, the second step is a falling transition $|2\rangle \rightarrow |0\rangle$, and the third step is another transition $|0\rangle \rightarrow |2\rangle$with the absorption of a probe photon $\boldsymbol{E}_3$. The last transition is $|2\rangle \rightarrow |0\rangle$, which emits an FWM photon at frequency ω_1. The corresponding multi-dressed Liouville pathway in such case is

$$\text{(F1)}\ \ \rho_{00}^{(0)} \xrightarrow{(\boldsymbol{E}_1)^*} \rho_{20}^{(1)} \xrightarrow{(\boldsymbol{E}_1')^*} \rho_{00}^{(2)} \xrightarrow{\boldsymbol{E}_3} \rho_{20}^{(3)}$$

$$\text{(F3)}\ \ \rho_{00}^{(0)} \xrightarrow{\boldsymbol{E}_2} \rho_{20}^{(1)} \xrightarrow{(\boldsymbol{E}_1')^*} \rho_{00}^{(2)} \xrightarrow{\boldsymbol{E}_3} \rho_{20}^{(3)}$$

The expression of the density-matrix element related to such multi-dressed $\boldsymbol{E}_{\rm F1}$ and $\boldsymbol{E}_{\rm F3}$ can be obtained as

$$\rho_{\rm F1}^{(3)} = \frac{-{\rm i}G_3G_1(G_1')^*}{\Gamma_{00}+\frac{|G_1|^2}{d_1}+\frac{|G_1|^2}{d_3}+\frac{|G_2|^2}{d_2}+\frac{|G_2|^2}{d_4}} \times\frac{1}{\left(d_1+\frac{|G_1|^2}{\Gamma_{00}+|G_2|^2/d_2}+\frac{|G_1|^2}{\Gamma_{22}}+\frac{|G_2|^2}{d_5}\right)^2} \tag{1a}$$

$$\rho_{\rm F3}^{(3)} = \frac{-{\rm i}G_3G_2(G_1')^*}{\left(d_7+\frac{|G_2|^2}{d_3}+\frac{|G_1|^2}{d_2}\right)\left(d_2+\frac{|G_2|^2}{\Gamma_{22}}+\frac{|G_2|^2}{\Gamma_{00}}+\frac{|G_1|^2}{d_6}\right)^2} \tag{1b}$$

where $d_1=\Gamma_{20}+{\rm i}\Delta_1$, $d_2=\Gamma_{20}+{\rm i}\Delta_2$, $d_3=\Gamma_{02}-{\rm i}\Delta_1$, $d_4=\Gamma_{02}-{\rm i}\Delta_2$, $d_5=\Gamma_{22}+{\rm i}(\Delta_1-\Delta_2)$, $d_6=\Gamma_{22}+{\rm i}(\Delta_2-\Delta_1)$, $d_7=\Gamma_{00}+{\rm i}(\Delta_2-\Delta_1)$, $\Delta_1=\Omega_{20}-\omega_1$ and $\Delta_2=\Omega_{20}-\omega_2$.

On the other hand, there exist two types of fluorescence signals due to spontaneous emission of photons from the upper levels, which can be described by the Liouville pathway:

$$\text{(R1)}\ \rho_{00}^{(0)} \xrightarrow{G_1} \rho_{10}^{(1)} \xrightarrow{(G_1)^*} \rho_{11}^{(2)}, \text{ and}$$

$$\text{(R2)}\ \rho_{00}^{(0)} \xrightarrow{\omega_2} \rho_{20}^{(1)} \xrightarrow{\omega_2^*} \rho_{00}^{(2)} \xrightarrow{\omega_1} \rho_{20}^{(3)} \xrightarrow{\omega_1^*} \rho_{22}^{(4)}$$

The expression of the density-matrix elements related to such multi-dressed R1 can be obtained as

$$\rho_{22}^{(2)} = \frac{G_1^2}{\left(d_1+\frac{|G_1|^2}{\Gamma_{00}}+\frac{|G_2|^2}{d_8}\right)\left(\Gamma_{22}+\frac{|G_2|^2}{d_2}+\frac{|G_1|^2}{d_1}\right)} \tag{1c}$$

$$\rho_{22}^{(4)} = \frac{G_1^2G_2^2}{\Gamma_{00}\left(d_2+\frac{|G_1|^2}{d_7}+\frac{|G_2|^2}{\Gamma_{00}}\right)\left(d_1+\frac{|G_1|^2}{\Gamma_{00}}+\frac{|G_2|^2}{d_8}\right)} \times\frac{1}{\Gamma_{22}+|G_1|^2\left(\frac{1}{d_1}+\frac{1}{d_3}\right)+|G_2|^2\left(\frac{1}{d_2}+\frac{1}{d_4}\right)} \tag{1d}$$

where $d_8=\Gamma_{00}+{\rm i}(\Delta_1-\Delta_2)$.

For the probe transmission, the Liouville pathway is $\rho_{00}^{(0)} \xrightarrow{G_3} \rho_{20}^{(1)}$, and we can obtain the first-order density matrix element as

$$\rho_{20}^{(1)} = \frac{{\rm i}G_3}{d_1+\frac{|G_1|^2}{\Gamma_{00}+|G_2|^2/d_2}+\frac{|G_1|^2}{\Gamma_{00}}+\frac{|G_1|^2}{\Gamma_{22}}+\frac{|G_2|^2}{d_5}} \tag{1e}$$

the imaginary part of which proportionally determines the absorption of probe beam in propagation.

2.2 Dressed state theory in the three V-level atomic system

The DFWM process in this three-level atomic system [as shown in Fig. 1(b)] can be described by the perturbation chain:

$$\text{(F1)}\ \rho_{00}^{(0)} \xrightarrow{(\boldsymbol{E}_1)^*} \rho_{20}^{(1)} \xrightarrow{(\boldsymbol{E}_1')^*} \rho_{00}^{(2)} \xrightarrow{\boldsymbol{E}_3} \rho_{20}^{(3)}$$

and the corresponding density matrix elements is

$$\rho_{\rm F1}^{(3)} = \frac{-{\rm i}G_3G_1(G_1')^*}{\Gamma_{00}+\frac{|G_1|^2}{d_1}+\frac{|G_1|^2}{d_3}+\frac{|G_2|^2}{d_2'}+\frac{|G_2|^2}{d_4'}} \times\frac{1}{\left(d_1+\frac{|G_1|^2}{\Gamma_{00}+|G_2|^2/d_2'}+\frac{|G_1|^2}{\Gamma_{11}}+\frac{|G_2|^2}{d_9}\right)^2} \tag{2a}$$

where $d_2'=\Gamma_{10}+{\rm i}\Delta_2$, $d_4'=\Gamma_{01}-{\rm i}\Delta_2$, $d_9=\Gamma_{21}+{\rm i}\Delta_1-{\rm i}\Delta_2$, $\Delta_1=\Omega_{20}-\omega_1$ and $\Delta_2=\Omega_{10}-\omega_2$.

Four transition paths that generate fluorescence signals can be described by perturbation chains:

$$\text{(R1)}\ \rho_{00}^{(0)} \xrightarrow{\omega_1} \rho_{20}^{(1)} \xrightarrow{\omega_1^*} \rho_{22}^{(2)}$$

$$\text{(R2)}\ \rho_{00}^{(0)} \xrightarrow{\omega_2} \rho_{10}^{(1)} \xrightarrow{\omega_2^*} \rho_{11}^{(2)}$$

$$\text{(R3)}\ \rho_{00}^{(0)} \xrightarrow{\omega_2} \rho_{10}^{(1)} \xrightarrow{\omega_2^*} \rho_{00}^{(2)} \xrightarrow{\omega_1} \rho_{20}^{(3)} \xrightarrow{\omega_1^*} \rho_{22}^{(4)}$$

$$\text{(R4)}\ \rho_{00}^{(0)} \xrightarrow{\omega_1} \rho_{20}^{(1)} \xrightarrow{\omega_1^*} \rho_{00}^{(2)} \xrightarrow{\omega_2} \rho_{10}^{(3)} \xrightarrow{\omega_2^*} \rho_{11}^{(4)}$$

with the corresponding density matrix elements being

$$\rho_{11}^{(2)} = \frac{G_2^2}{\left(d_1'+\frac{|G_1|^2}{\Gamma_{00}}\right)\left(\Gamma_{00}+\frac{|G_2|^2}{d_2}\right)} \tag{2b}$$

$$\rho_{22}^{(2)} = \frac{G_1^2}{\left(d_2+\frac{|G_2|^2}{\Gamma_{00}}\right)\left(\Gamma_{00}+\frac{|G_1|^2}{d_1'}\right)} \tag{2c}$$

$$\rho_{11}^{(4)} = \frac{G_1^2G_2^2}{\Gamma_{00}\left(\Gamma_{11}+\frac{|G_1|^2}{d_1'}+\frac{|G_1|^2}{d_3'}\right)\left(d_1'+\frac{|G_1|^2}{\Gamma_{00}}\right)\left(d_2+\frac{|G_2|^2}{\Gamma_{00}}\right)} \tag{2d}$$

$$\rho_{22}^{(4)} = \frac{G_1^2G_2^2}{\Gamma_{00}\left(\Gamma_{11}+\frac{|G_2|^2}{d_2}+\frac{|G_1|^2}{d_3}\right)\left(d_1'+\frac{|G_1|^2}{\Gamma_{00}}\right)\left(d_2+\frac{|G_2|^2}{\Gamma_{00}}\right)} \tag{2e}$$

where $d_1'=\Gamma_{10}+{\rm i}\Delta_1$ and $d_3'=\Gamma_{01}-{\rm i}\Delta_1$.

For the probe transmission, the Liouville pathway is $\rho_{00}^{(0)} \xrightarrow{G_3} \rho_{20}^{(1)}$, and the corresponding density matrix ele-

ments is

$$\rho_{20}^{(1)} = \frac{\mathrm{i}G_3}{d_1 + \frac{|G_1|^2}{\Gamma_{00}+|G_2|^2/d_2'} + \frac{|G_1|^2}{\Gamma_{00}} + \frac{|G_2|^2}{d_9}} \tag{2f}$$

In our experiment, the sodium vapor is an EIT-enhanced Kerr medium. The mathematical description of the propagation properties of $\boldsymbol{E}_{3,\mathrm{F1}}$ with the self- and cross-Kerr nonlinearities induced by the control and pump beams ($\boldsymbol{E}_2$, $\boldsymbol{E}_2'$, $\boldsymbol{E}_1$, and $\boldsymbol{E}_1'$) can be obtained through numerically solving the following coupled equations:

$$\begin{aligned}
&\frac{\partial u_3}{\partial Z} - \frac{\mathrm{i}\partial^2 u_3}{2\partial\xi^2} - \frac{\mathrm{i}\partial^2 u_3}{2\partial\eta^2} \\
&\quad = \frac{\mathrm{i}k_3^2 w_0 I}{n_0}(n_2^{S1}|u_3|^2 + 2n_2^{X1}|u_1|^2 \\
&\qquad + 2n_2^{X2}|u_1'|^2 + 2n_2^{X3}|u_2|^2 + 2n_2^{X4}|u_2'|^2)u_3 \qquad (3a) \\
&\frac{\partial u_{\mathrm{F1}}}{\partial Z} - \frac{\mathrm{i}\partial^2 u_{\mathrm{F1}}}{2\partial\xi^2} - \frac{\mathrm{i}\partial^2 u_{\mathrm{F1}}}{2\partial\eta^2} \\
&\quad = \frac{\mathrm{i}k_{\mathrm{F1}}^2 w_0^2 I}{n_0}(n_2^{S2}|u_{\mathrm{F1}}|^2 + 2n_2^{X5}|u_1|^2 + 2n_2^{X6}|u_1'|^2 \\
&\qquad + 2n_2^{X7}|u_2|^2 + 2n_2^{X8}|u_2'|^2)u_{\mathrm{F1}} \qquad (3b)
\end{aligned}$$

where $Z = z/L_D$ ($L_D = k_1 w_0^2$ is the diffraction length and ω_0 the spot size); z is the longitudinal coordinate in the beam propagation direction, $k_3 = k_{\mathrm{F1}} = \omega_1 n_0/c$; n_0 is the linear refractive index at ω_1; n_2^{S1-S2} are the self-Kerr coefficients of $\boldsymbol{E}_{3,\mathrm{F1}}$; $n_2^{X1-X8}$are the cross-Kerr coefficients of $\boldsymbol{E}_{3,\mathrm{F1}}$ induced by $\boldsymbol{E}_1$, $\boldsymbol{E}_1'$, $\boldsymbol{E}_2$ and $\boldsymbol{E}_2'$, which are given by a general expression $n_2 \approx \mathrm{Re}\tilde{\rho}_{20}^{(3)}/(\varepsilon_0 c n_0)$, is negative for self-defocusing and positive for self-focusing, and $\tilde{\rho}_{20}^{(3)}$ can be obtained from the coupled density-matrix equations. The notations $\xi = x/w_0$ and $\eta = y/w_0$ are the transversal dimensionless coordinates; $u_{3,\mathrm{F1}} = A_{3,\mathrm{F1}}/I^{1/2}$, $u_{1,2} = A_{1,2}/I^{1/2}$ and $u_{1,2}' = A_{1,2}'/I^{1/2}$ are the normalized amplitudes of the beams $\boldsymbol{E}_{3,\mathrm{F1}}$, $\boldsymbol{E}_{1,2}$ and $\boldsymbol{E}_{1,2}'$, with I donating the intensity.

3 Experimental results and theoretical analyses

3.1 Dressed signals in two-level systems

The probe transmission, FWM signals and fluorescence signals with different Δ_1 in the two level system are shown in Fig. 2(a), (c) and (e), respectively. And Fig. 2(b), (d) and (f) are the corresponding theoretical simulations. As depicted by the dotted lines in Fig. 2(a1)–(a5), the shifting dip in the probe transmission alters from EIA, to flat line, and again to EIA, and meanwhile moves from right to left, which corresponds to Δ_1 varying from positive to negative. We can find the probe transmission is asymmetry at $\Delta_1 = 0$, i.e., the height of the EIT peak in $\Delta_1 > 0$ is smaller than that in $\Delta_1 < 0$. In Fig. 2(c1)–(c5), we present the FWM signal, which conclude NDFWM and the DFWM simultaneously, in which we can see a shifting emission peak of NDFWM and a fixed suppression dip of DFWM. The phenomenon matches well with that shown in Fig. 2(a). As for the fluorescence signal as shown in Fig. 2(e), there is always sa single-photon emission peak with a suppression dip at $\Delta_2 = 0$. Our numerics agree well with our experiments.

The explanations of these effects lie in the density matrix element related to these signals in Eq. (1). $|G_1|^2/[\Gamma_{00} + |G_2|^2/(\Gamma_{20} + \mathrm{i}\Delta_2)]$, which interacts with $|G_1|^2/\Gamma_{22}$ cascadely, can dress the probe transmission only when Δ_2 is scanned under the two-photon resonant-like (or EIT like) condition $\Delta_1 - m\Delta_2 = 0$, where $m = G_1/G_2$. If $m > 1$, $\Delta_2 = \Delta_1/m$ will move the position of EIT close to $\Delta_2 = 0$, while if $m < 1$, EIT moves far away from $\Delta_2 = 0$. Thus, the dressing effect of $\boldsymbol{E}_2$ ($\boldsymbol{E}_2'$) can be modulated by $\boldsymbol{E}_1(\boldsymbol{E}_1')$ through the parameter m. So, for the probe transmission, one EIA due to $G_2^2/[\Gamma_{22} + \mathrm{i}(\Delta_1 - \Delta_2)]$ moves from right to left as shown by the dashed line in Fig. 2(a). Another EIA around Δ_2=0 is due to $|G_1|^2/[\Gamma_{00} + |G_2|^2/(\Gamma_{20} + \mathrm{i}\Delta_2)]$, and the EIT within the EIA dip in the negative area is probably due to the cascade interaction mentioned above. We just consider $|G_1|^2/[\Gamma_{00} + |G_2|^2/(\Gamma_{20} + i\Delta_2)]$ in the theoretical analysis with the corresponding EIA condition $\Delta_1 - m(\Delta_2 \pm \lambda_{G_2\pm}) = 0$. As shown in Fig. 2(g), we find that the separation between the dressed energies becomes narrower if $m > 1$ and wider if $m <$1. Actually, the evolution of FWM from EIA, flat line to EIA was obtained for different Δ_1 by scanning Δ_2 in our recent work [17]. And the related density matrix elements are shown in Eqs. (1a) and (1b). With Δ_1 scanned, $|G_1|^2/(\Gamma_{10} + \mathrm{i}\Delta_1)$ and $|G_1|^2/(\Gamma_{02} - \mathrm{i}\Delta_1)$ in Eq. (1a), $|G_2|^2/(\Gamma_{20} - \mathrm{i}\Delta_1)$ in Eq. (1b) are all single-photon dressing terms, and same results can be obtained for $|G_2|^2/(\Gamma_{20} + \mathrm{i}\Delta_2)$ and $|G_2|^2/(\Gamma_{02} - \mathrm{i}\Delta_2)$ in Eq. (1a), $|G_1|^2/(\Gamma_{20} + \mathrm{i}\Delta_2)$ in Eq. (1b) if Δ_2 is scanned. Because $\boldsymbol{E}_1$ and $\boldsymbol{E}_2$ are in the same direction, the two-photon Doppler-free conditions will be satisfied for the two level systems, thus the signals due to two-photon or two-photon-like resonances are dominant, so the signals due to single-photon dressing terms can not be observed. Now it is clear that the shifting emission peak of NDFWM is due to $\Gamma_{00} + \mathrm{i}(\Delta_2 - \Delta_1)$ in Eq. (1b), and the fixed suppression dip of DFWM is due to $|G_1|^2/[\Gamma_{00} + |G_2|^2/(\Gamma_{20} + \mathrm{i}\Delta_2)]$.

The asymmetric phenomena mentioned above can be explained by the transition resonant frequency between $3\mathrm{P}_{3/2}$ and hyperfine energy levels $F = 1$ and $F = 2$ of the ground-state $3\mathrm{S}_{1/2}$. In Fig. 1(a), the center of mass

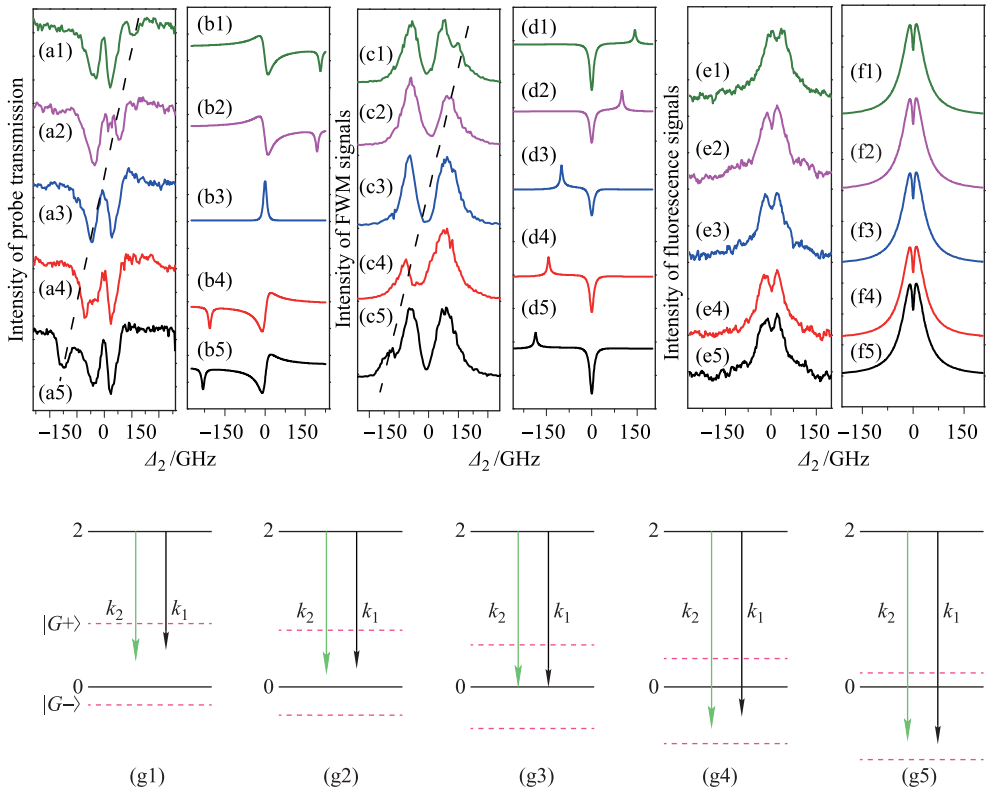

Fig. 2 **(a)**, **(c)** and **(e)** Measured evolution of the probe transmission, FWM signals and fluorescence signals versus Δ_2 in two-level ($|0\rangle - |2\rangle$) systems, for $\Delta_1 = 100.6$ GHz, 74.6 GHz, 0 GHz, −78 GHz, –100.1 GHz, from (1) to (5), respectively. The dotted lines in (a) and (c) represents the shift trace of the characteristic regions in the spectrum. **(b)**, **(d)** and **(f)** Theoretical plots corresponds to (a), (c) and (e), respectively. **(g)** The dressed-state pictures of the DFWM signal. $|G+\rangle$ and $|G-\rangle$: two dressed states caused by the field $E_2(E_2')$.

locates at the place where the distance from $F = 2$ is 3/8 of that between F=1 and F=2. When $\Delta_i < 0$, the dipole moment μ_i here is smaller than that with $\Delta_i > 0$. Thus, $G_2 = \mu_2 E_2/\hbar$ is larger in $\Delta_i > 0$, and the dressing effect becomes weaker due to $|G_1|^2/[\Gamma_{00} + |G_2|^2/(\Gamma_{20} + \mathrm{i}\Delta_2)]$. For the fluorescence signal, the emission peak is due to $\Gamma_{20} + \mathrm{i}\Delta_2$, and the suppression contribution can be depicted by $|G_2|^2/(\Gamma_{20} + \mathrm{i}\Delta_2)$ in Eq. (1c)–(1d).

3.2 Dressed signals in V type-level system

Next, we investigate the evolutions of the probe transmission, DFWM, and fluorescence signals with different Δ_1 in a V-type three-level system with $\boldsymbol{E}_2$ and $\boldsymbol{E}_2'$ driving $|0\rangle - |1\rangle$. When Δ_1 goes from positive to negative, the result of the evolution of the probe transmission versus Δ_2 is similar with that in Fig. 2(a), which is due to $|G_1|^2/[\Gamma_{00} + |G_2|^2/(\Gamma_{20} + \mathrm{i}\Delta_2)]$ in Eq. (2f).

In this V-type three-level system, only DFWM is obtained as shown in Fig. 3(c), and it is almost pure-suppression for most of Δ_1 values. However, the height of the signal in Fig. 3(c4)–(c5) is larger than that in Fig. 3(c1)–(c2). Similar to the cases in two-level systems, the corresponding suppression condition is $\Delta_1 - m\Delta_2 = 0$ due to the multi-dressing term $|G_1|^2/[\Gamma_{00} + |G_2|^2/(\Gamma_{20} + \mathrm{i}\Delta_2)]$ in Eq. (3e). In the experiment, $m = G_1/G_2 > 1$ is still satisfied and the dressed energy states on the same side with $\Delta_1 > 0$ are squeezed. However, the powers of $\boldsymbol{E}_1$ ($\boldsymbol{E}_1'$) and $\boldsymbol{E}_2$ ($\boldsymbol{E}_2'$) are much larger than those in former experiments that the pure-suppression of the FWM signal can be observed for most of Δ_1 values. For the fluorescence signal in Fig. 3(e1)–(e5), the emission peak is due to the single-photon emission term $\Gamma_{20} + \mathrm{i}\Delta_2$ in Eq. (2b)–(2d). And the suppression dip on the peak is due to the dressing effects of $\boldsymbol{E}_2$ from $|G_2|^2/(\Gamma_{20} + \mathrm{i}\Delta_2)$ in Eq. (2a) and (2b).

3.3 Comparison of dressed signals in two and V-type three-level systems

Here in this part, we compare the spectra of probe transmission signal, two coexisting DFWM signals and fluorescence signals with different Δ_1 as shown in Fig. 4(a)–(c) in two different energy level systems [Fig. 4(d1) and (d2)] with the wavelength $\lambda_1 = 588.8$ nm and the detuning Δ_2 being scanned from driving $|0\rangle - |2\rangle$ to $|0\rangle - |1\rangle$. The probe transmission signal with two EIAs is shown in Fig. 4(a1)–(a8), and when Δ_i ($i = 1, 2$) is negative, the

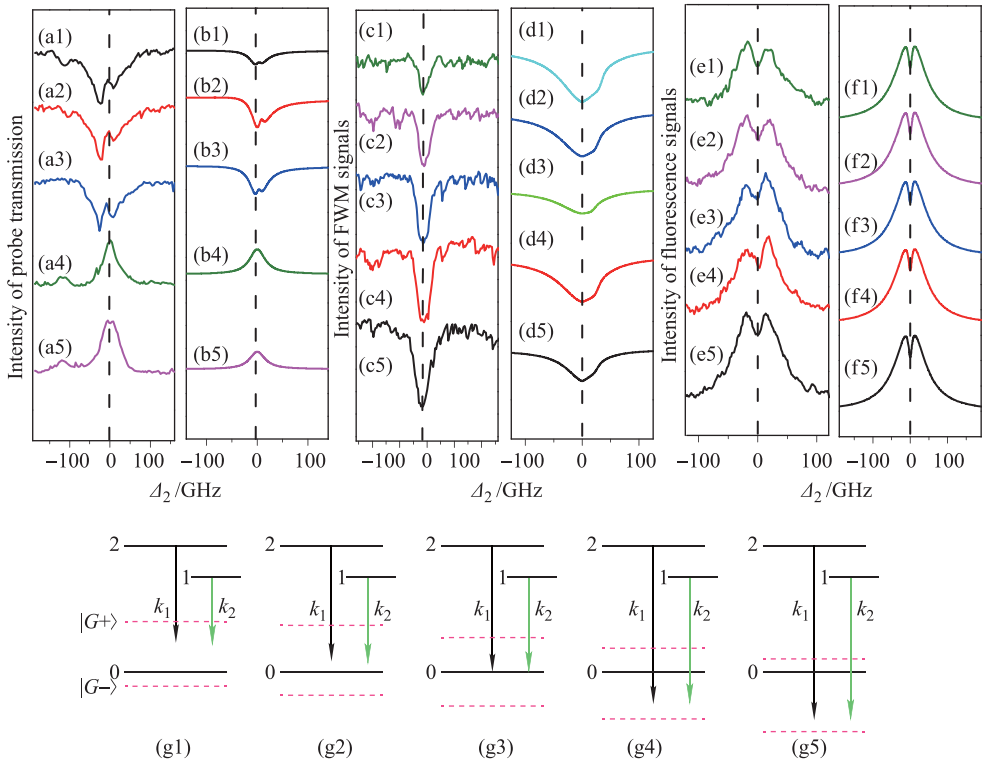

Fig. 3 **(a)**, **(c)** and **(e)** Measured evolution of the probe transmission, the DFWM signals and fluorescence signals versus Δ_2 with (a1) $\Delta_1 = 97.7$ GHz, (a2) $\Delta_1 = 32.2$ GHz, (a3) $\Delta_1 = 0$ GHz, (a4) $\Delta_1 = -28.5$ GHz, (a5) $\Delta_1 = -80.2$ GHz, , respectively in V-type energy-level system as shown in Fig. 1(c). **(b)**, **(d)** and **(f)** Theoretical results correspond to (a), (c) and (e). **(g1)**–**(g5)** The dressed-state pictures of the suppression and enhancement of the DFWM signal. $|G+\rangle$ and $|G-\rangle$: two dressed states caused by the field $E_2(E_2')$.

atomic level diagram is depicted by Fig. 4(d1), where Δ_1 is in $|0\rangle - |2\rangle$ transition and Δ_2 is scanned through this transition. The generated left EIA (named P1) is consistent with the EIA from two-level system in Fig. 2(a), and the right EIA (named P2) is consistent with that from three-level system in Fig. 3(a). In Fig. 4(a1)–(a8), it is clear to see that P1 is deeper than P2. This phenomenon can be explained that μ_i in the region of $\Delta_2 > 0$ is smaller than that in the region of $\Delta_2 < 0$. Due to $G_2 = \mu_2 E_2/H$, G_2 with $\Delta_2 < 0$ is larger and the cascade multi-dressing interaction between $|G_1|^2/[\Gamma_{00} + |G_2|^2/(\Gamma_{20} + i\Delta_2)]$ and $|G_1|^2/\Gamma_{11}$ in Eq. (2f) is stronger.

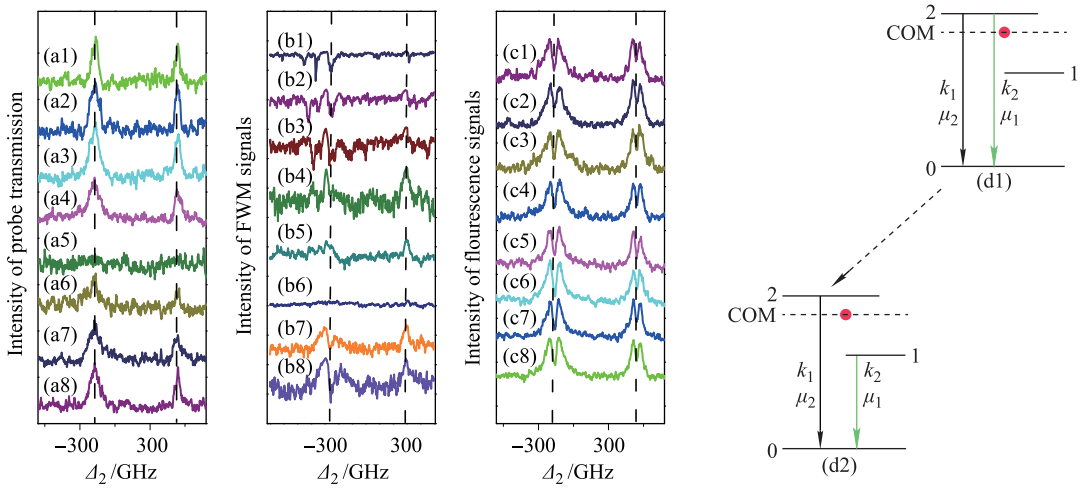

Fig. 4 **(a)**, **(b)** and **(c)** Measured evolution of the probe transmission, the two coexisting DFWM signals and fluorescence signals versus Δ_2 with (a1) $\Delta_1 = 338.5$ GHz, (a2) $\Delta_1 = 292.6$ GHz, (a3) $\Delta_1 = 255.6$ GHz, (a4) $\Delta_1 = 218.2$ GHz, (a5) $\Delta_1 = 177.3$ GHz, (a6) $\Delta_1 = 136.4$ GHz, (a7) $\Delta_1 = 98.5$ GHz, (a8) $\Delta_1 = 46.2$ GHz, respectively. **(d1)**–**(d2)** Atomic levels diagrams, in which the center of mass in four different energy level types are marked out as the horizontal dashed lines and labeled as COM, respectively The signals in (a)–(c) are distributed according to the distribution of the energy levels in (d).

Under the same experimental condition, each curve in Fig. 4(b) depicts two coexisting DFWM signals. The locations of DFWM signals (named F1, F2 respectively) are consistent with those of the probe transmission. One can see that F1 is stronger than F3 in Fig. 4(b1)–(b8), which is also because of the stronger dressing effect of transition $|0\rangle - |2\rangle$. As to the fluorescence signal [see Fig. 4(c1)–(c8)], the depth of the suppression dip and height of the emission peak are determined by the dressing effects and the dipole moment, respectively, which is similar as the probe transmission signals and the DFWM signals.

3.4 Changing the angle of the dressing fields in two-level system

Finally, we study intensities and spatial properties of signals by changing the angle of dressing fields in a two-level system, as shown in the Fig. 1(a). Under the same experimental condition, for an hot atom with velocity υ along angular bisector of the pump fields, the frequency of $\boldsymbol{E}_2$ (or $\boldsymbol{E}_2'$) shifts to $\omega_2 - \boldsymbol{k}_2\upsilon\cos(\theta_{2y}/2)$ phenomenally considering the Doppler effect on the weak signals. For probe $\boldsymbol{E}_3$ signal, the single-photon absorption peak arises at $\Delta_1 = 0$ depicted by the right dashed line in Fig. 5(a). Moreover, the EIT window arises around $\Delta_1 = -20$ GHz and corresponding EIA dip are depicted by the left dashed curve in Fig. 5(a). For $\boldsymbol{E}_{\rm F1}$, in Fig. 5(c), the primary A–T splitting at $\Delta_1 = 0$ and secondary one around $\Delta_1 = -20$ GHz are obtained. Also, $\Delta\theta_2$ is changed from -0.15 to 0.15, these signals around $\Delta_1 = -20$ GHz change correspondingly with the strongest value at $\Delta\theta_2 = 0$. First, for the probe $\boldsymbol{E}_3$ signal, when Δ_1 is scanned, the single-photon absorption dip arises at $\Delta_1 = 0$ due to $\mathrm{i}\Delta_1 + \Gamma_{20}$ in Eq. (1e) and the EIT window at $\Delta_1 = -20$ GHz where the two-photon resonance condition $\Delta_1 - \Delta_2' = 0$ determined the two-photon dressing term $|G_2|^2/[\Gamma_{22}+\mathrm{i}(\Delta_1-\Delta_2')]$ is satisfied, where $\Delta_2' = \Delta_2 + k_2\upsilon\cos(\theta_{2y}/2)$, as shown in Fig. 5(b). Then, for $\boldsymbol{E}_{\rm F1}$ signal, as shown in Fig. 5(d), by scanning Δ_1 the one-photon emission peak forms by $\mathrm{i}\Delta_1 + \Gamma_{10}$ in Eq. (1a). The primary A–T splitting at $\Delta_1 = 0$ is induced by the terms $|G_1|^2/[\Gamma_{00} + |G_1|^2/(\Gamma_{20} + \mathrm{i}\Delta_1)]$ and $|G_3|^2/[\Gamma_{22}+|G_1|^2/(\Gamma_{20}+\mathrm{i}\Delta_1)]$ in Eq. (1a). The secondary A–T splitting at around $\Delta_1 = -20$ GHz is caused by the term $|G_2|^2/[\Gamma_{00}+\mathrm{i}(\Delta_1-\Delta_2')]$ due to the two-photon resonant condition $\Delta_1 - \Delta_2' = 0$. When $\Delta\theta_2$ changes from -0.15 to 0.15, the detuning of $\boldsymbol{E}_2$ and $\boldsymbol{E}_2'$ changes with

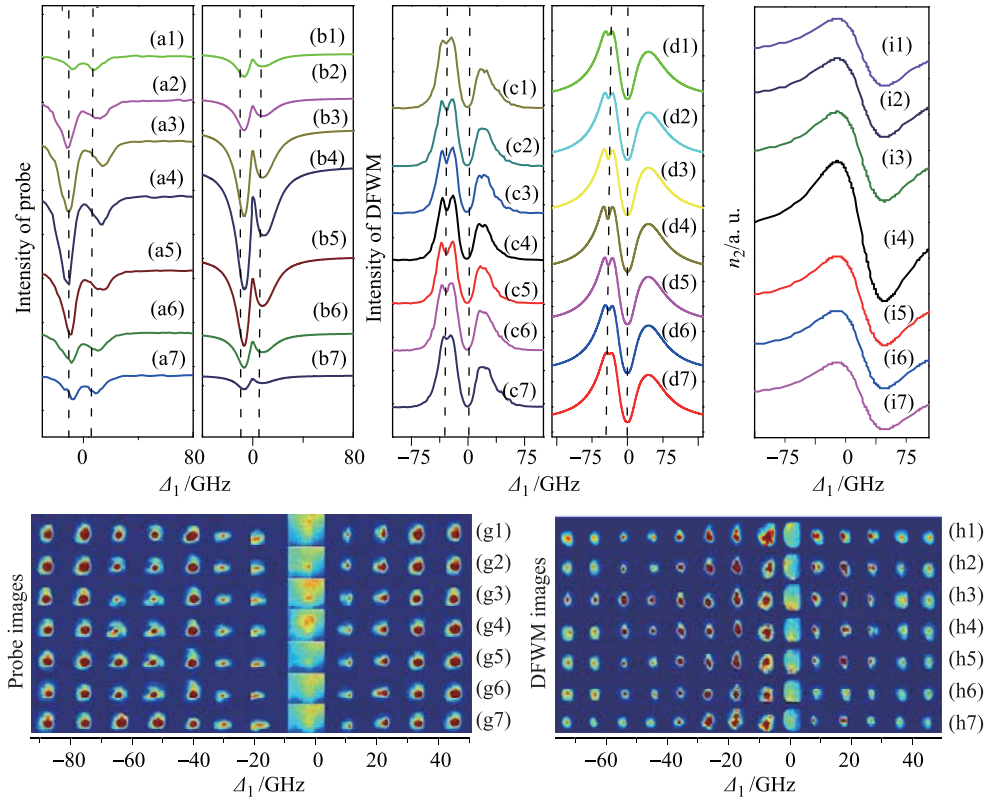

Fig. 5 **(a)** and **(c)** show the experimentally measured intensities of the probe and FWM versus Δ_1, respectively, with $\Delta_2 = -20$ GHz in a two-level system. From (1) to (7), $\Delta\theta_2$ increases by 0.15 from -0.15. And the involved powers are $G_1 = G_1' = 1.2$ GHz, $G_3 = 0.3$ GHz and $G_2 = G_2' = 1.1$ GHz. **(b)** and **(d)** show the theoretically calculated intensities of the probe and FWM respectively versus Δ_1 corresponding to (a), (c). **(g)** and **(h)** Images of $\boldsymbol{E}_3$ and $\boldsymbol{E}_{\rm F1}$. **(i)** The theoretical Kerr nonlinear coefficient $\boldsymbol{n}_2$ of $\boldsymbol{E}_2$ ($\boldsymbol{E}_2'$).

$\Delta\theta_2$ due to $\Delta_2' = \Delta_2 + k_2 v\cos(\theta_{2y}/2)$, thus, the dressing effect of $\boldsymbol{E}_2$ ($\boldsymbol{E}_2'$) on $\boldsymbol{E}_3$ and $\boldsymbol{E}_{\rm F1}$ signals also changes with $\Delta\theta_2$. What's more, the dressing effect is the strongest at $\Delta\theta_2 = 0$.

In addition, the images of $\boldsymbol{E}_3$ and $\boldsymbol{E}_{\rm F1}$ beams induced by XPM are recorded at different $\Delta\theta_2$ by scanning Δ_1 from negative to positive, as shown in Fig. 5(g) and (h). Curves in Fig. 5(i) are the corresponding numerical simulations of nonlinear index n_2 versus $\Delta\theta_2$ under the dressing effect of $\boldsymbol{E}_2$ and $\boldsymbol{E}_2'$ near $\Delta_1 = -20$ GHz.

Figure 5(g4) [Fig. 5(h4)] can be obtained when $\Delta\theta_2 = 0$ is fixed and Δ_1 is scanned, and the images of $\boldsymbol{E}_3(\boldsymbol{E}_{\rm F1})$ show significant focusing takes up around the EIA windows [see Fig. 5(a)] in the region $\Delta_1 < 0$, in which n_2 is positive and arrives its maximum, as shown in the Fig. 5(i4). However, with Δ_1 increasing gradually, $\boldsymbol{E}_3(\boldsymbol{E}_{\rm F1})$ images evolve from focusing to defocusing, because n_2 varies from positive (in $\Delta_1 < 0$) to negative (in $\Delta_1 > 0$). When $|\Delta\theta_2|$ changes from 0 to 0.15, the focusing and defocusing phenomena due to the crossing Kerr nonlinearity from $\boldsymbol{E}_2$ and $\boldsymbol{E}_2'$ become weaker gradually, as shown in Fig. 5(g1)–(g3) [Fig. 5(h1)–(h3)] and Fig. 5(g5)–(g7) [Fig. 5(h5)–(h7)]. In order to explain the above experimental results, we perform the nonlinearity coefficient n_2 due to $\boldsymbol{E}_2$ and $\boldsymbol{E}_2'$, depending on the angle $\Delta\theta_2$, can be expressed as $n_2 \propto \tilde{\rho}_{10}^{(3)} = -{\rm i}G_3G_1G_1'^*/[(d_1 + |G_2|^2/d_{10})^2(\Gamma_{00} + |G_2|^2/d_{11})]$, where $d_{10} = \Gamma_{00} + {\rm i}(\Delta_1 - \Delta_2')$ and $d_{11} = \Gamma_{20} + {\rm i}\Delta_2'$. Therefore, with angle $|\Delta\theta_2|$ increasing [from Fig. 2(i1) to (i7)], we can see $|n_2|$ decreases and reaches its maximum at $\Delta\theta_2 = 0$. So the focusing and defocusing effect are most significant at $\Delta\theta_2 = 0$. The experimental results have reasonable agreement with the theoretical ones.

4 Conclusion

To summarize, we have analyzed and made a thorough comparison among the probe transmission, FWM and fluorescence signals observed in V-type three-level and two-level atomic systems. Meanwhile, we present the interesting results that both the hyperfine structure and transition dipole moment can all affect the dressing effect. Theoretical simulations agree with the experimental results very well. In addition, we have also investigated the spatial properties of FWM by changing the angles between dressing fields in two-level atomic systems, including focusing/defocusing effect, which have been well explained by the cross-Kerr nonlinear effect. The research in this paper may have potential applications in signal processing and help people understand the controllable spatial pattern formation and dynamics.

Acknowledgements This work was supported by the National Basic Research Program of China (973 Program) (Grant No. 2012CB921804) and the National Natural Science Foundation of China (Grant Nos. 10974151, 61078002, 61078020, 11104214, 61108017, 11104216, and 61205112).

References

1. S. E. Harris, Phys. Today, 1997, 50(7): 36
2. P. R. Hemmer, D. P. Katz, J. Donoghue, M. Cronin-Golomb, M. S. Shahriar, and P. Kumar, Opt. Lett., 1995, 20(9): 982
3. B. Lu, W. H. Burkett, and M. Xiao, Opt. Lett., 1998, 23(10): 804
4. A. S. Zibrov, A. B. Matsko, O. Kocharovskaya, Y. V. Rostovtsev, G. R. Welch, and M. O. Scully, Phys. Rev. Lett., 2002, 88(10): 103601
5. S. W. Du, J. M. Wen, M. H. Rubin, and G. Y. Yin, Phys. Rev. Lett., 2007, 98(5): 053601
6. Y. Zhang, B. Anderson, A. W. Brown, and M. Xiao, Appl. Phys. Lett., 2007, 91(6): 061113
7. M. D. Lukin, S. F. Yelin, M. Fleischhauer, and M. O. Scully, Phys. Rev. A, 1999, 60(4): 3225
8. M. Yan, E. G. Rickey, and Y. F. Zhu, Phys. Rev. A, 2001, 64(1): 013412
9. Z. Q. Nie, H. B. Zheng, P. Z. Li, Y. M. Yang, Y. P. Zhang, and M. Xiao, Phys. Rev. A, 2008, 77(6): 063829
10. Y. P. Zhang, Z. Q. Nie, Z. G. Wang, C. B. Li, F. Wen, and M. Xiao, Opt. Lett., 2010, 35(20): 3420
11. C. B. Li, H. B. Zheng, Y. P. Zhang, Z. Q. Nie, J. P. Song, and M. Xiao, Appl. Phys. Lett., 2009, 95(4): 041103
12. A. J. Stentz, M. Kauranen, J. J. Maki, G. P. Agrawal, and R. W. Boyd, Opt. Lett., 1992, 17(1): 19
13. H. Wang, D. Goorskey, and M. Xiao, Phys. Rev. Lett., 2001, 87(7): 073601
14. P. Li, Z. Zhao, Z. Wang, Y. Zhang, H. Lan, H. Chen, H. Zheng, and Y. Zhang, Appl. Phys. Lett., 2012, 101(8): 081107
15. Y. Wu, Phys. Rev. A, 2005, 71(5): 053820
16. Z. Y. Zhao, Z. G. Wang, P. Y. Li, G. P. Huang, N. Li, Y. Q. Zhang, Y. Q. Yan, and Y. P. Zhang, Laser Phys. Lett., 2012, 9(5): 802
17. Y. P. Zhang, U. Khadka, B. Anderson, and M. Xiao, Phys. Rev. Lett., 2009, 102(1): 013601